Research Square

Preprints are preliminary reports that have not undergone peer review.
They should not be considered conclusive, used to inform clinical practice,
or referenced by the media as validated information.

Plasmonic anchoring boosts mechanoluminescence via mechano–electro–optical cascade

Guoyan Dong

gydong@ucas.ac.cn

University of Chinese Academy of Sciences https://orcid.org/0000-0003-3389-2642

Yutao Qin

University of Chinese Academy of Sciences

Jiaxiang He

University of Chinese Academy of Sciences

Haonan Shi

State Key Laboratory of New Ceramic Materials, Tsinghua University

Xueli Sun

University of Chinese Academy of Sciences

Zheng Zhu

University of Chinese Academy of Sciences

Wengao Tang

University of Chinese Academy of Sciences

Tianzhuo Zhao

University of Chinese Academy of Sciences https://orcid.org/0000-0002-0369-7558

Ji Zhou

Tsinghua University

Article

Keywords:

Posted Date: November 4th, 2026

DOI: https://doi.org/10.21203/rs.3.rs-11378559/v1

License: This work is licensed under a Creative Commons Attribution 4.0 International License.
Read Full License

Additional Declarations: There is no conflict of interest

Plasmonic anchoring boosts mechanoluminescence via mechano–electro–optical cascade

Yutao Qin[1], Jiaxiang He[1], Guoyan Dong[1]*, Haonan Shi[2,3], Xueli Sun[1], Zheng Zhu[1], Wengao Tang[1], Tianzhuo Zhao[1,4]*, and Ji Zhou[2,3]*

[1]School of Optoelectronics, University of Chinese Academy of Sciences, Beijing 101408, China

[2]State Key Laboratory of New Ceramic Materials, Tsinghua University, Beijing 100084, China

Full list of author information is available at the end of the article

These authors contributed equally: Yutao Qin and Jiaxiang He

*Correspondence: Guoyan Dong (gydong@ucas.ac.cn) or Tianzhuo Zhao (zhaotianzhuo@ucas.ac.cn) or Ji Zhou (zhouji@tsinghua.edu.cn)

Abstract

Localized surface plasmon resonance has been extensively exploited to enhance photoluminescence and electroluminescence, yet its application to mechanoluminescence remains unrealized due to the metal-induced quenching-enhancement trade-off and irreversible interfacial delamination under cyclic strain. Here we report the first plasmonically enhanced ML elastomer via an in-situ reduction strategy that anchors ~70 nm Au nanoparticles directly onto ZnS:Cu phosphors through covalent Au–S bonds within a PDMS matrix. This interfacial architecture simultaneously passivates sulfur-vacancy quenching centers and confines the LSPR near-field within the carrier-detrapping zone, accelerating radiative recombination via the Purcell effect. Concurrently, the covalent Au–S dipole establishes an “electronic lock” that temporally gates carrier release, mitigating non-radiative losses. Au incorporation alone boosts ML brightness (~6-fold) and mechano–optical sensitivity

(~5.5-fold). When integrated with Al_2O_3 stress concentrators, a synergistic mechano–electro–opticall cascade achieves ~9-fold enhancement at 20 wt% phosphor loading, with exceptional cyclic stability (2.78% fluctuation over 600 cycles). This platform circumvents the long-standing quenching-durability dilemma, enabling self-powered strain mapping, wearable stress monitoring, and intuitive human-machine interfaces. Our work establishes a generalizable interfacial design paradigm for plasmon-enhanced mechanophotonic devices.

Keywords: mechanoluminescence; localized surface plasmon resonance; Purcell enhancement; Au–S covalent anchoring; interfacial engineering; triboelectric nanogenerator; soft optoelectronics

Introduction

Mechanoluminescence (ML) represents a unique transduction pathway that converts ambient mechanical energy directly into optical signals without external power supplies or optical excitation[1-3]. This inherent self-powered capability establishes ML materials as a cornerstone technology for real-time stress visualization[4], structural health monitoring and interactive human-machine interfaces [5-7]. Among diverse ML materials, ZnS:Cu-based composites stand out for wearable sensing applications owing to their bright green emission, environmental robustness and compatibility with flexible polymer matrices[7-10]. Recent researches highlight the rapid transition from traditional ML powders to advanced mechanoplasmonic hybrid systems for next-generation sensing[11].

The ML mechanism in ZnS:Cu is generally attributed to triboelectric-field-induced electron detrapping from sulfur-vacancy (V_S) donor states, followed by radiative

recombination at Cu^+ acceptor centers[8,12]. Its quantum efficiency is fundamentally limited by non-radiative decay pathways through deep trap states and interfacial defects. In conventional ZnS:Cu/PDMS composites, a large fraction of mechanically generated charge carriers recombine non-radiatively before reaching luminescent Cu^+ sites, leading to intrinsically low ML brightness under weak mechanical stimuli. Furthermore, repeated loading-unloading cycles inherent to elastomer operation inevitably induce interfacial degradation: rigid ceramic or metallic fillers gradually delaminate from the soft polymer matrix, causing irreversible emission decay[13,14].

To address these efficiency and durability limitations, multiple enhancement strategies have been developed across distinct structural levels. At the material level, phosphor host optimization focuses on tuning doping/co-doping concentrations to increase emissive center density[8], engineering trap depths via controlled annealing, and constructing micro-heterojunctions to promote directional charge transfer and suppress interfacial recombination[5,12]. At the device level, piezotronic and ferroelectric coupling strategies exploit built-in fields to lower carrier detrapping barriers[15], as exemplified by PVDF-encapsulated ML layers[16] where induced piezoelectric field reduces trap depths and accelerates carrier release, and ZnO-based heterojunctions that leverage strong piezoelectric polarization for field-assisted electron emission[5]. At the matrix level, dispersing rigid inorganic nanoparticles (e.g., SiO_2[13], $Sr_3(BO_3):Pr^{3+}$ [8] or Al_2O_3[3]) into soft elastomers concentrates local shear stress and thereby amplifies the interfacial triboelectric potential. Despite substantial progress, each approach remains constrained by intrinsic drawbacks: chemical doping cannot overcome the limit of carrier replenishment under continuous cyclic loading[8]; piezotronic/ferroelectric coupling requires complex multilayer fabrication incompatible with straightforward composite processing[16]; high rigid filler loadings inevitably stiffen the elastomer, reduce fracture

toughness and induce irreversible mechano–optical (M–O) fatigue[14].

Localized surface plasmon resonance (LSPR)[17] of noble metal nanostructures offers a promising paradigm to bypass these limitations. Intense localized electromagnetic fields supported by Au/Ag nanostructures markedly accelerate the radiative recombination rate of adjacent luminescent centers via the Purcell effect[18-20], fundamentally distinct from conventional carrier-density or trap-depth modulation. While LSPR has been extensively exploited to enhance photoluminescence[21,22] and electroluminescence[23], its application to ML remains unrealized. This research gap stems from the quenching-enhancement trade-off from uncontrolled metal-phosphor distance[22,24] and irreversible interfacial delamination[23,24]. On the one hand, uncontrolled metal-phosphor proximity causes quenching, while excessive distance renders the LSPR near-field ineffective. On the other hand, cyclic deformation drives irreversible interfacial delamination due to Young's modulus mismatch between different fillers, invalidating any physical spacing strategy.

In this work, we report the first demonstration of plasmonically enhanced ML achieved by in-situ growing Au nanoparticles (NPs) covalently anchored on ZnS:Cu via Au–S bonds within PDMS. The curing-agent-mediated in-situ reduction strategy has recently emerged as a robust route for embedding plasmonic nanostructures within elastomeric networks[25]. This covalent anchoring simultaneously passivates quenching centers[26], positions the LSPR near-field within the carrier-detrapping zone for Purcell enhancement[11,27], and creates an interfacial dipole that gates carrier release. Co-embedded Al_2O_3 stress concentrators further amplify triboelectric charge generation, delivering a synergistic mechano–electro–opticall (M–E–O) cascade. This dual-filler elastomer delivers a record ~9-fold ML enhancement at an ultra-low phosphor loading (20 wt%) while preserving the host matrix flexibility. Benefiting from robust Au–S

covalent anchoring, the composite exhibits excellent fatigue resistance with only 2.78% intensity fluctuation over 600 continuous deformation cycles. This work establishes a universal physical framework for plasmonic-triboelectric coupling in soft ML composites and provides a robust design paradigm for next-generation self-powered optical sensors and interactive smart skins[28,29].

Results

In-Situ Fabrication and Microstructural Characterization

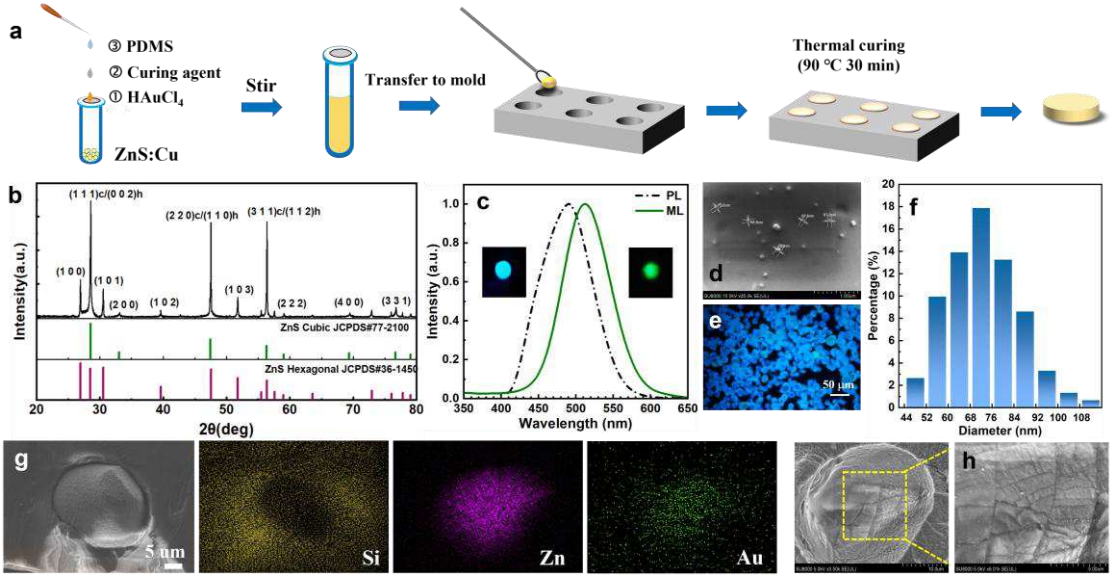


Fig. 1 In-situ fabrication and microstructural characterization of Au-decorated ZnS:Cu/PDMS hybrid elastomers. **a** Schematic of in-situ reduction synthesis route using Si–H bond reduction of $HAuCl_4$ in the presence of ZnS:Cu and PDMS. **b** XRD pattern of pristine ZnS:Cu showing mixed cubic zinc blende and hexagonal wurtzite phases. **c** Normalized PL (400 nm excitation) and ML spectra showing a ~20 nm redshift relative to PL. **d** SEM image of in-situ reduced Au NPs ($HAuCl_4$ precursor of 7.8 μmol L^{-1}) within PDMS matrix. **e** Fluorescence micrograph of 20 wt% ZnS:Cu/PDMS film upon 400 nm UV excitation. **f** Statistical particle size distribution of the in-situ reduced Au NPs. **g** EDS elemental mapping of the Au/ZnS:Cu/PDMS hybrid material, and the corresponding EDS spectrum shown in Fig. S3. **h** High-magnification SEM showing Au nanoparticles selectively decorating ZnS:Cu surfaces.

A facile in-situ reduction routine was developed to realize the decoration of Au nanoparticles (NPs) on the ZnS:Cu surface. As schematically depicted in Fig. 1a, ZnS:Cu phosphor powder (Fig. S2) was first premixed with an ethanolic $HAuCl_4$ solution. Subsequently, the PDMS curing agent was added to the slurry, followed by stirring for 5 min. The active Si–H bonds in the curing agent drive the in-situ chemical reduction of Au^{3+} ions to form metallic Au NPs. Next, the PDMS prepolymer was introduced at a prepolymer-to-curing agent weight ratio of 10:1, and the mixture was further homogenized to ensure uniform distribution of all components. Finally, the homogeneous mixture was cast into polytetrafluoroethylene (PTFE) molds and cured at 90 °C for 30 min in a forced-air oven to form a crosslinked polymer network, yielding the final composite samples.

X-ray diffraction (XRD) was performed to characterize the crystal structure of the active phosphors (Fig. 1b). The diffraction peaks are in good agreement with both the cubic zinc blende (JCPDS No. 77–2100) and hexagonal wurtzite (JCPDS No. 36–1450) phases of ZnS[30], confirming a mixed-phase polycrystalline nature. Quantitative phase analysis reveals that the cubic and hexagonal phases account for approximately 79% and 21% of the total, respectively, with no detectable CuO, CuS, or other secondary impurity phases. Notably, the phase junctions and stacking faults between the cubic and hexagonal domains serve as abundant carrier trap sites in this mixed-phase structure. The low content of the non-centrosymmetric hexagonal (piezoelectric) phase indicates that conventional piezoelectric-field-induced carrier release is not the dominant pathway for ML excitation[31]. Instead, the ML behavior is driven by a triboelectric process at the ZnS:Cu/PDMS elastomeric interfaces, where the sliding phase boundaries generate high-density electrostatic fields that induce carrier detrapping[32]. The average crystallite size of the ZnS:Cu phosphor was estimated from the (111)

diffraction peak using the Scherrer equation[33]

$$D = \frac{k\lambda}{\beta \cos\theta} \quad (1)$$

where D is the mean crystallite size, k is the shape factor (taken as 0.89), λ is the X-ray wavelength (0.15406 nm for Cu Kα radiation), β is the full width at half maximum (FWHM) in radians after instrumental broadening correction, and θ is the Bragg diffraction angle. Using the measured FWHM of 0.084° (0.00147 rad) for the (111) peak, the average crystallite size was calculated to be ~96.2 nm. This nanoscale crystalline domain structure generates a high density of grain boundaries and defect centers, facilitating efficient carrier trapping and subsequent triboelectric-field-driven detrapping[34].

The emission characteristics of the hybrid composite under mechanical and optical excitation are presented in Fig. 1c. Upon excitation at 400 nm, the normalized steady-state PL spectrum exhibits a broad emission band centered at 490 nm. This emission is ascribed to the donor-acceptor pair (DAP) radiative recombination: electrons transit from the conduction band or shallow sulfur-vacancy V_s donor states to the ground state of the copper-associated acceptor (the t_2 level of Cu^+) within the undisturbed tetrahedral ZnS host lattice[35]. Under mechanical loading (stretching or compression), the ML spectrum exhibits a single green emission band centered at ~510 nm. This pronounced ~20 nm redshift relative to the PL emission reflects fundamentally distinct charge excitation and radiative-decay mechanisms. Whereas PL originates from optical absorption-driven interband excitation under static equilibrium, ML is driven by localized band tilting under dynamic triboelectric (and minor piezoelectric) fields, which lowers potential barriers and facilitates quantum tunneling of deeply trapped electrons from V_s states. Subsequent recombination of these tunneling–detrapped electrons at stress-distorted lattice coordination sites consequently yields the redshifted

green ML emission at 510 nm.

The in-situ reduction of $HAuCl_4$ precursors to form monodispersed metallic Au NPs within the PDMS matrix was verified by scanning electron microscopy (SEM), as shown in Fig. 1d; the corresponding particle size distribution of an Au/PDMS film (without ZnS:Cu) is presented in Fig. 1e. At an $HAuCl_4$ concentration of 7.8 μmol L^{-1}, the discrete Au NPs exhibit a narrow size distribution with a mean diameter of ~70 nm (Fig. 1f). Energy-dispersive X-ray spectroscopy (EDS) elemental mapping (Fig. 1g) and high-magnification SEM imaging (Fig. 1h) were carried out to investigate the spatial distribution and interfacial architecture of the multicomponent ZnS:Cu/PDMS/Au system. The elemental maps of Si, Zn, and Au reveal that Au is not only uniformly dispersed throughout the bulk matrix but also exhibits distinct preferential accumulation at the interfaces surrounding ZnS:Cu microparticles.

The covalent Au–S anchoring firmly pins the Au NPs to the phosphor surfaces, aligning the LSPR near-field with the triboelectrically activated carrier-detrapping zone. Finite-Difference Time-Domain (FDTD) simulation and analytical modeling define the effective coupling window as ~10–30 nm from the interface (Supplementary Note 1). Within this regime, Au–S bonding chemically passivates surface sulfur vacancies[26], suppressing near-field quenching channels and shifting the metal–phosphor interaction balance toward net radiative enhancement. This defect-healing mechanism ensures that the localized plasmonic field efficiently accelerates radiative recombination via the Purcell effect, yielding a measurable optical gain as directly evidenced by the shortened ML lifetime and amplified emission intensity.

In-Situ Reaction Kinetics, Interfacial Electronic Offsets, and ML Mechanisms

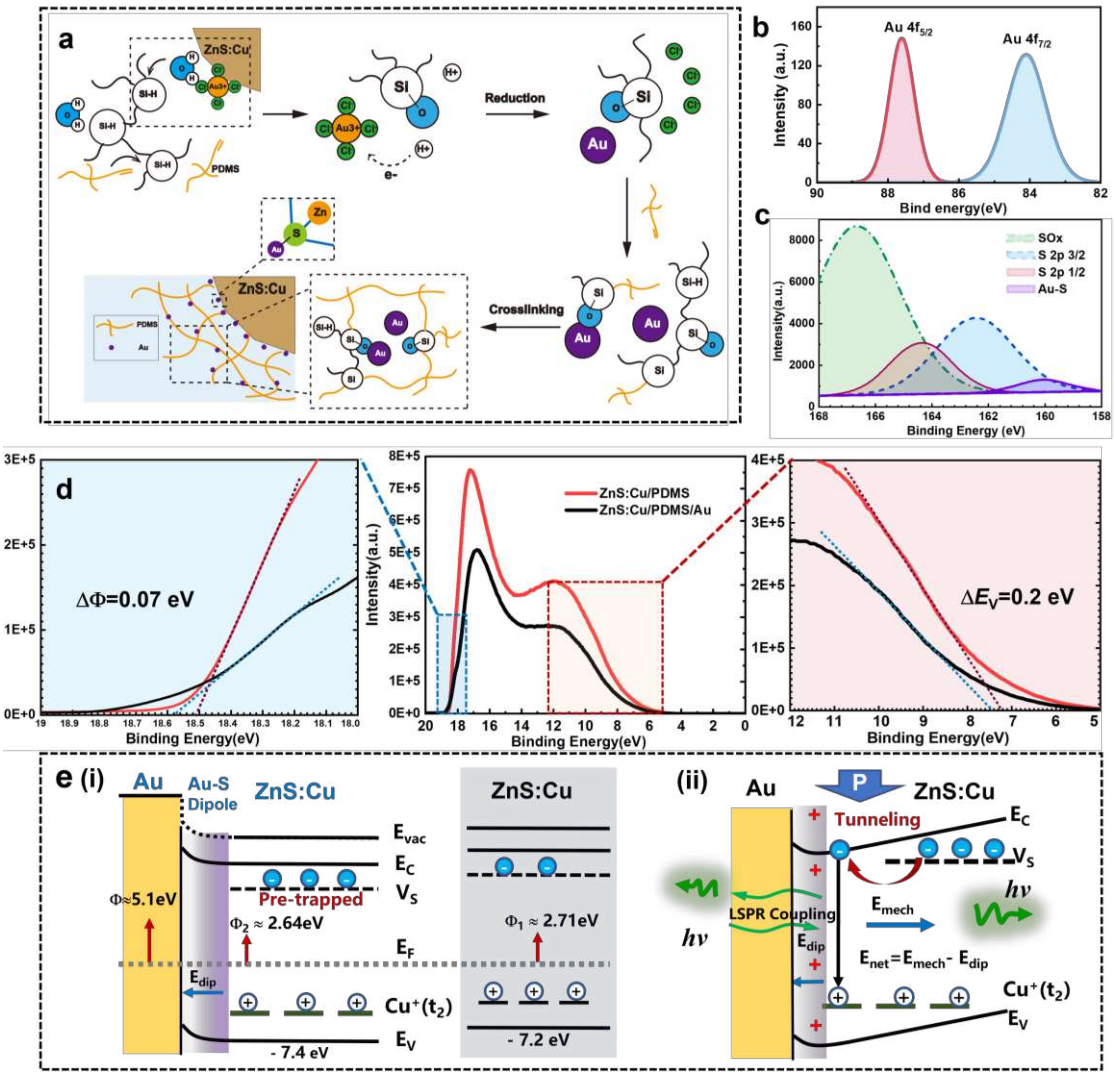


Fig. 2 Interfacial electronic structure analysis and ML mechanism. a Schematic of two-step Si–H hydrolysis and Au^{3+} reduction process, with steric hindrance from siloxane cross-linking restricting Au NP growth. **b** Au 4f XPS spectrum confirming fully reduced metallic Au^0. **c** S 2p XPS revealing Au–S coordination bonds at ~160 eV, confirming covalent anchoring of Au NPs on ZnS:Cu. **d** UPS spectra showing work function reduction upon Au anchoring, indicative of interfacial dipole reconstruction. **e** Energy-band diagrams of ML mechanism: (**i**) Energy band diagram of Au-decorating ZnS:Cu with the "electronic lock" by interfacial dipole field trapping carriers in V_s states, compared with that of the pristine under static conditions; (**ii**) Field-assisted quantum tunneling and Purcell-enhanced emission under dynamic compression.

To elucidate the origin of the synergistic ML enhancement, we systematically investigated the chemical reaction pathways underlying the in-situ reduction of Au NPs

in the ZnS:Cu/PDMS matrix, as well as the associated interfacial electronic interactions. The in-situ reduction, nucleation, and growth of Au NPs proceed[36] via two coupled sequential steps (Fig. 2a). In Step 1, upon mixing the ethanolic $HAuCl_4$ solution with the PDMS curing agent, the highly reactive hydrosilane (Si–H) groups in the curing agent undergo hydrolysis promoted by residual moisture originating from the $HAuCl_4$ precursor solution and ambient humidity[37]. This nucleophilic process drives the oxidation of Si–H bonds to silanol (Si–OH) groups, accompanied by the release of electrons and protons. In Step 2, the solvated $AuCl_4^-$ anions rapidly scavenge these liberated electrons at the interfaces, undergoing a quantitative reduction to metallic Au^0. During this redox-coupling process, the concurrent thermal cross-linking of the siloxane (Si–O–Si) network creates strong spatial steric hindrance, which restricts the long-range diffusion and Ostwald ripening of the freshly nucleated gold seeds. This dynamic pinning effect confines the average size (~70 nm) of the resulting Au NPs well within the nanoscale regime. Owing to the local charge inhomogeneities and sulfur-rich surface terminations of the ZnS:Cu microparticles, a substantial portion of the Au precursor is preferentially adsorbed onto the phosphor surfaces, consequently, yielding dense interfacial decoration on ZnS:Cu surfaces (Fig. 1g).

The high-resolution Au 4f X-ray photoelectron spectroscopy (XPS) spectrum (Fig. 2b) features a well-resolved spin-orbit doublet[38], with peaks centered at binding energies of 84.0 eV (Au $4f_{7/2}$) and 87.6 eV (Au $4f_{5/2}$). The observed 3.6 eV spin-orbit splitting is a characteristic spectroscopic signature of fully reduced metallic Au^0. Notably, no satellite peaks ascribed to high-valence Au^{3+} (typically located in the 85.5-86.5 eV range) are detected, corroborating the complete reduction of the Au precursor. The high-resolution S 2p XPS spectrum (Fig. 2c) further elucidates the nature of the interfacial coordination between Au NPs and the ZnS:Cu surface. The spectrum is

deconvoluted into a well-resolved spin-orbit doublet, with the S $2p_{3/2}$ and S $2p_{1/2}$ components centered at 162.4 eV and 164.5 eV, respectively, characteristic of the Zn-S bonding network within the host ZnS:Cu lattice[39]. Notably, an additional low-energy shoulder is clearly discernible at ~160 eV. In accordance with the hard-soft acid-base (HSAB) principle, metallic Au^0 exhibits a strong thermodynamic affinity for sulfide (S^{2-}) terminations at the ZnS:Cu surface[40,41]. This distinct low-energy spectral feature can therefore be assigned to chemisorbed Au–S coordination bonds, confirming that the Au NPs are chemically anchored onto the phosphor surfaces. Such robust chemical anchoring not only inhibits mechanical delamination of the metallic phase under cyclic elastomeric shear, but also constructs efficient conductive pathways for interfacial charge transport.

The interfacial electronic structures and energy-level alignments of the composites were systematically characterized via ultraviolet photoelectron spectroscopy (UPS) with He I excitation ($h\nu$ = 21.22 eV), as presented in Fig. 2d. For the pristine ZnS:Cu/PDMS sample, the secondary electron cut-off edge lies at 18.51 eV, and the valence band maximum ($E_{v\beta m}$), determined from the spectral onset, is -7.2 eV with respect to the Fermi level (E_F = 0 eV). This yields an intrinsic work function of Φ_1 = 2.71 eV. Upon in-situ Au NP anchoring, the secondary electron cut-off exhibits a distinct shift to 18.58 eV, corresponding to a reduced work function of the hybrid composite Φ_2 = 2.64 eV ($\Delta\Phi$ = 0.07 eV). Concurrently, $E_{v\beta m}$ shifts downward to -7.4 eV, verifying an overall 0.2 eV downward shift of the band structure relative to E_F. The mismatch between the magnitudes of $\Delta\Phi$ and $\Delta E_{v\beta m}$ ($|\Delta E_{v\beta m}| > |\Delta\Phi|$) cannot be rationalized by conventional metal-semiconductor contact models. Instead, this provides unambiguous evidence for interfacial electronic state reconstruction driven by strong covalent Au–S bonding at the heterointerface[42]. The covalent bonding at the

heterointerface gives rise to a highly localized interfacial dipole field (E_{dip}) oriented toward the Au NPs. Under static conditions (Fig. 2e(i)), this strong covalently induced E_{dip} acts as an "electronic lock": it induces a narrow depletion region near the ZnS:Cu surface, which stabilizes and pre-traps electron carriers in sulfur vacancy (V_s) defect states[41]. The upward band bending within this depletion region effectively suppresses non-radiative recombination and thermally activated carrier leaking, corresponding to the energy barrier effect introduced by in-situ Au anchoring.

The energy-band alignment under mechanical excitation is schematically illustrated in Fig. 2e(ii). Upon application of dynamic compressive stress, intense localized shear strain and interfacial sliding within the elastomer matrix cause the electronegative PDMS to accumulate negative surface charges (−σ), whereas the Au-anchored ZnS:Cu surfaces acquire positive charges (+σ). The elevated electric potential at the ZnS:Cu generates a strong built-in electric field (E_{mech}) directed from the ZnS:Cu surface toward the bulk, inducing a pronounced downward tilt of the energy bands. The superposition of E_{mech} and E_{dip} narrows the effective tunneling and activation barrier, enabling rapid liberation of pre-trapped electrons from V_s states via field-assisted quantum tunneling, followed by direct transition to the conduction band. Concurrently, the anchored Au NPs serve as localized charge and field concentrators, amplifying the local electrostatic gradient and thereby lowering the threshold energy for trap-to-band electron detrapping. While a fraction of the detrapped electrons recombine with $Cu^+(t_2)$ luminescent centers to produce the characteristic emission at $h\nu$ = 510 nm, the majority are driven toward and spatially confined at the highly polarized interface, circumventing non-radiative trapping or premature quenching.

During the subsequent release phase, the applied mechanical pressure is abruptly withdrawn. E_{mech} collapses instantaneously, whereas the covalently stabilized E_{dip}

remains intact, leading to an abrupt reduction in the net electric field and lifting of the localized barrier confinement. Consequently, the large population of conduction-band electrons previously accumulated and stored at the interface are immediately released from the spatial trapping potential, and rapidly drift and diffuse back into the bulk of ZnS:Cu, triggering an avalanche of radiative recombination with the $Cu^{+}(t_2)$ acceptor states. The radiative recombination of this carrier surge (~510 nm) is further enhanced via the Purcell effect arising from LSPR coupling of the anchored Au NPs, which positions the near-field within the carrier-detrapping zone for maximal light-matter interaction. Since the release phase functions as a gating mechanism that discharges all the stored carriers in a concentrated burst within a millisecond-scale time window, the ML intensity during release is inherently higher and sharper than that during the compressing phase.

Composition-Dependent ML and Plasmonic Enhancement

The ML spectral, time-resolved measurements, and single-pulse impact apparatus (Fig. 3a) were used to explore the M–E–O conversion law. Phosphor-free Au-PDMS control samples, prepared over a wide concentration gradient of $HAuCl_4$ precursor, were used as a baseline reference. At an ultra-low concentration of 7.8 μmol L^{-1}, the absorption curve of the Au-PDMS sample is nearly indistinguishable from the pure PDMS baseline, which accounts for the high transparency for the UCAS badge under the first sample in Fig. 3b. With increasing precursor concentrations (from 7.8×10^{-5} to 3.9×10^{-2} mol L^{-1}), the samples progressively transition from highly transparent to deep purple. The peak absorbance in the UV-vis spectra increases by approximately two orders of magnitude, complying with the Beer-Lambert law[43]. Crucially, the characteristic LSPR absorption peak remains stable, consistently falling within the 511-517 nm range. This well-defined absorption band spectrally overlaps with the intrinsic

ML emission of ZnS:Cu (~510 nm), establishing an optimal spectral matching condition for strong plasmonic near-field coupling.

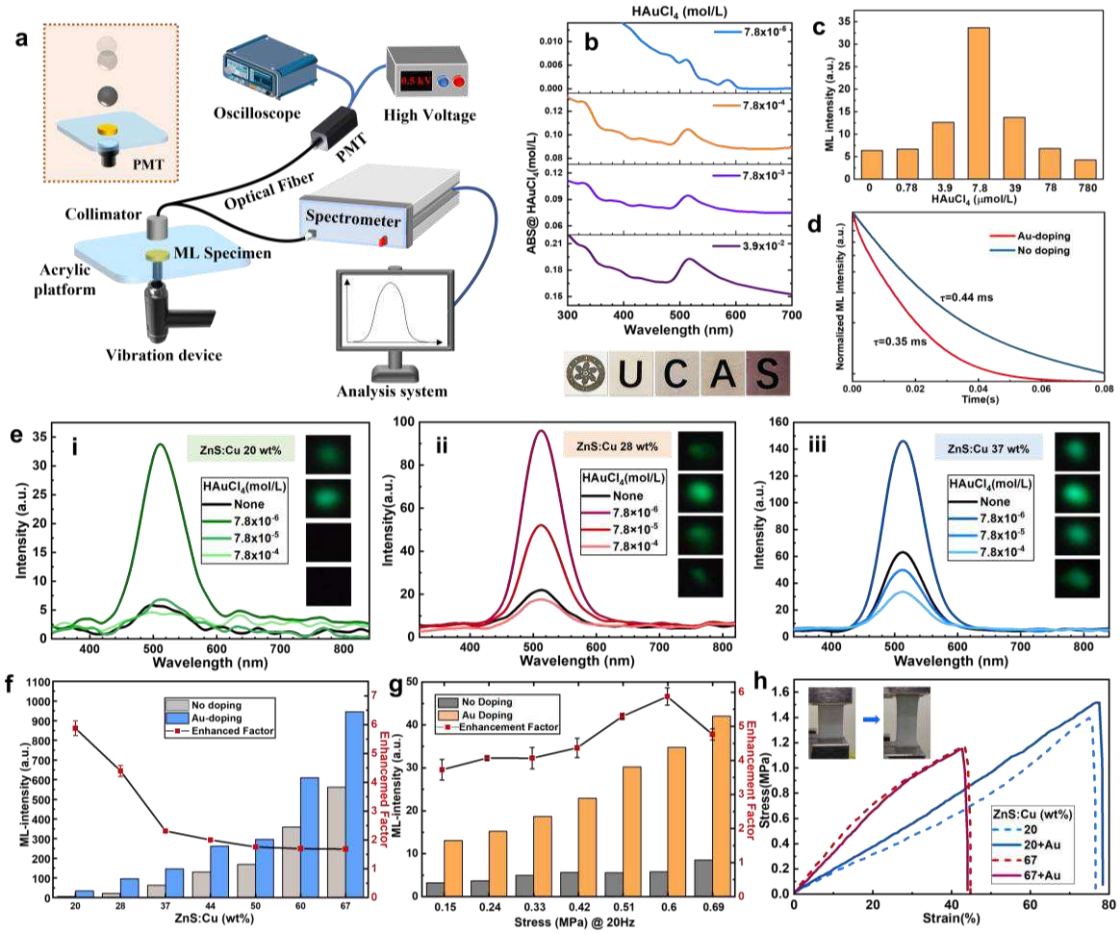


Fig. 3 Composition-dependent ML enhancement and M–O sensitivity. a Schematics of ML spectral, time-resolved measurement, and single-pulse impact apparatus. **b** UV-vis absorption spectra and corresponding photographs of Au-PDMS films with varying $HAuCl_4$ concentrations. **c** ML intensity versus $HAuCl_4$ concentration showing a volcano-shaped trend with the peak at 7.8 μmol L^{-1} (20 wt% ZnS:Cu, 0.60 MPa). **d** ML transient decay curves of pristine and Au-doped samples, showing shortened lifetime (0.44 ms to 0.35 ms) and Purcell factor $F_P > 1.26$. **e** ML spectra of hybrid discs under compressive loading (0.6MPa) as the functions of ZnS:Cu mass (20, 28, 37 wt%) and $HAuCl_4$ concentration (0-780 μmol L^{-1}), with insets corresponding to excited-state luminescence images. **f** Au-doped (7.8 μmol L^{-1}) ML intensities (histograms) and enhancement factor (red squares) versus different ZnS:Cu loadings (20-67 wt%). **g** ML intensity (histograms) and enhancement factor (red squares) versus applied stress (0.15-0.69 MPa at 20 Hz). **h** Stress–strain

curves of pristine (dashed lines) and Au-doped (solid lines) samples (size 20×10×1 mm) of 20 wt% and 67 wt% ZnS:Cu loadings, showing preserved elastomeric compliance.

Unless otherwise noted, all dynamic ML measurements presented hereafter were performed under a uniform periodic compressive stimulus of 0.6 MPa at 20 Hz to ensure a consistent testing baseline. Using disc samples (10 mm diameter × 1 mm thickness) with a fixed baseline loading of 20 wt% ZnS:Cu, we investigated the dependence of steady-state ML peak intensity on the Au precursor concentration, showing a characteristic volcano-shaped trend (Fig. 3c). As the $HAuCl_4$ concentration rises to the optimal 7.8 μmol L^{-1}, the ML peak intensity increases monotonically, delivering a ~6-fold enhancement relative to the baseline of the pristine Au-free ZnS:Cu/PDMS. This volcano-shaped trend reflects the competition between plasmonic enhancement and non-radiative quenching: at low Au loading, increasing LSPR hotspot density drives higher ML output, while excessive Au NPs induce metal-induced quenching and Ohmic dissipation that suppress emission.

Time-resolved ML decay measurements were performed under single-pulse impact excitation delivered by a synchronized steel-ball drop apparatus (the inset in Fig. 3a), to elucidate the origin of plasmonic ML enhancement in the optimized hybrid sample (20 wt% ZnS:Cu, 7.8 μmol L^{-1} $HAuCl_4$). In Fig. 3d, the transient luminescence decay curves reveal a pronounced shortening of effective carrier lifetime (τ) upon Au incorporation, with the ML decay lifetime decreasing from 0.44 ms for the pristine film to 0.35 ms for the Au-anchored composite. The experimental Purcell factor F_p is rigorously defined as the enhancement of the local density of optical states (LDOS):

$$F_P = \frac{\Gamma_{rad}}{\Gamma_{rad,0}} = \frac{\tau_0}{\tau} \cdot \frac{\eta}{\eta_0} \quad (2)$$

where Γ_{rad} is the radiative decay rate, τ the measured lifetime, and η the internal

quantum yield. The shortened ML lifetime (0.44 → 0.35 ms) yields an apparent Purcell factor of $F_P^{app} = \tau_0 / \tau \approx 1.26$. Since Au–S covalent anchoring simultaneously passivates surface non-radiative traps and enhances radiative decay, the true quantum yield satisfies $\eta > \eta_0$[44]. Consequently, F_P^{app} represents a conservative lower bound for the actual Purcell enhancement, confirming that LSPR coupling dominantly accelerates radiative recombination and markedly enhances the overall luminescence emission efficiency of the composite. As directly evidenced by the volcano-shaped concentration dependence and shortened ML lifetime, the optimal Au loading guarantees that plasmonic near-field enhancement and Purcell-accelerated radiative recombination overwhelmingly dominate over parasitic absorption and Ohmic dissipation, satisfying the condition for efficient dipole-plasmon coupling.

In Fig. 3e, we further exmined the enhancement effect of Au NPs across varying ZnS:Cu mass fractions (20 wt%, 28 wt%, and 37 wt%) at different $HAuCl_4$ precursor concentrations. The $HAuCl_4$ dosage is normalized to the ZnS:Cu phosphor mass (0.13 mL g^{-1}) to ensure uniform surface coverage of Au NPs on individual phosphor particles across all formulations. This calibration keeps the average areal density of in-situ reduced Au NPs on each ZnS:Cu microparticle consistent, thus isolating the effect of phosphor loading from changes in the local LSPR environment (with detailed compositions in Table S1). The corresponding ML spectra (with inset photographs of emissive samples) show that the absolute ML intensity scales with increasing ZnS:Cu loading. Across all three filler contents, the optimized Au precursor concentration (7.8 μmol L^{-1}) consistently yields the maximum ML output.

However, the relative enhancement factor (the ratio of ML peak intensity with and without Au, Fig. 3f, solid curve) decreases with the increasing phosphor loading. Specifically, the factor drops from ~6-fold at 20 wt% ZnS:Cu to ~1.8-fold at 67 wt%

loading. The declining relative enhancement at high phosphor loadings does not reflect a weakened plasmonic mechanism, but rather stems from a steeply rising baseline ML intensity driven by increased emitter density and intensified inter-particle mechanical contacts. Concurrently, four interrelated factors attenuate the relative gain: (i) elevated matrix stiffness (Young's modulus increases from ~1.5 to ~3.5 MPa) restricts elastic deformation, thereby diminishing the triboelectric charge density per unit stress; (ii) the reduced polymer fraction promotes Au NP aggregation, enhancing non-radiative Ohmic damping; (iii) dense particle packing induces near-field plasmonic coupling between adjacent Au-decorated phosphors, spectrally detuning the LSPR resonance from the 510 nm emission band; and (iv) prolonged photon transport paths in the densely packed network exacerbate parasitic scattering and reabsorption losses[45]. Collectively, these effects suppress the relative enhancement factor while the absolute plasmonic gain remains largely preserved.

Next, the M–O transduction sensitivity of the optimized hybrid disc (20 wt% ZnS:Cu, 7.8 μmol L^{-1} Au precursor) across a stress range from 0.15 to 0.69 MPa was evaluated at the fixed frequencies of 20 Hz (Fig. 3g), 25 (Fig. S4a), and 30 Hz (Fig. S4b). The ML intensity of both pristine and Au-incorporated samples increases monotonically with applied stress, with the Au-doped delivering significantly higher absolute output across the entire range. More importantly, the Au-doped hybrid exhibits ~5.5-fold enhancement in M–O sensitivity, rising from 9.78 a.u./MPa for the pristine sample to 53.67 a.u./MPa for the Au-doped hybrid at 20 Hz, ~ 5.05-fold at 25 Hz, and ~4.38-fold at 30 Hz. A direct consequence of LSPR Purcell effect is to amplify each mechanically generated carrier into a higher-rate radiative recombination event. This substantially improved sensitivity makes the hybrid material highly attractive for low-stress tactile sensing applications where small pressure changes must be transduced into clearly

detectable optical signals. The relative intensity enhancement factor (red squares in Fig. 3g) peaks near 0.60 MPa and remains 4~6-fold amplification across the 0.15-0.69 MPa span, confirming that the LSPR Purcell enhancement operates robustly over a wide pressure window. The synergistic combination of stable enhancement and high sensitivity establishes a reliable M–O transduction pathway, positioning the hybrid elastomer as a platform for wide-dynamic-range tactile sensing.

The hybrid elastomers retain excellent mechanical compliance across varying phosphor loadings, as evidenced by the tensile stress–strain curves in Fig. 3h. At the optimized ultra-low Au precursor concentration (7.8 μmol L^{-1}), plasmonic modification imposes a negligible mechanical penalty. The 20 wt% ZnS:Cu composite maintains a low Young's modulus of ~1.5 MPa , while increasing the rigid filler content to 67 wt% raises the modulus to ~3.5 MPa. Crucially, covalent Au–S anchoring localizes trace Au NPs at the phosphor interface, preserving the continuity of the cross-linked PDMS network and circumventing the interfacial debonding and embrittlement typical of physically blended composites. This interfacial design effectively decouples optical enhancement from mechanical degradation, enabling high-brightness ML output without compromising the intrinsic elasticity of the soft matrix.

Dynamic ML Behavior and M–E–O Cascade Boost in Hybrid Elastomers

Dynamic ML properties of the pristine (20 wt%) and co-optimized Au-doped (7.8 μmol L^{-1}) hybrid samples were evaluated using a photomultiplier tube (PMT) to record transient optical output signals under periodic mechanical stimuli (Fig. 4a). Each cycle of different compressive loads (0.43, 0.52, and 0.61 MPa) at 20 Hz exhibits a characteristic double-peak waveform: a lower loading peak during compression and a sharp high unloading peak during stress release. This double-peak profile is a hallmark of the contact-separation triboelectric mechanism in phosphor-elastomer composites,

where the loading and unloading phases generate distinct interfacial charge dynamics[46]. During compression, PDMS viscous damping causes a progressive contact-warmup, allowing carriers to tunnel from V_s trap states (Fig. 2e(ii)) in a gradual manner and yielding a broader, lower peak. During stress release, the instantaneous viscoelastic snapback of the elastomer generates an abrupt collapse of the interfacial electric field, triggering synchronized release of carriers accumulated at the interface and producing a sharp, intense emission burst. The Au-doped sample's unloading peak is significantly taller and narrower than the pristine control—a direct kinetic signature of Purcell-enhanced radiative recombination[47].

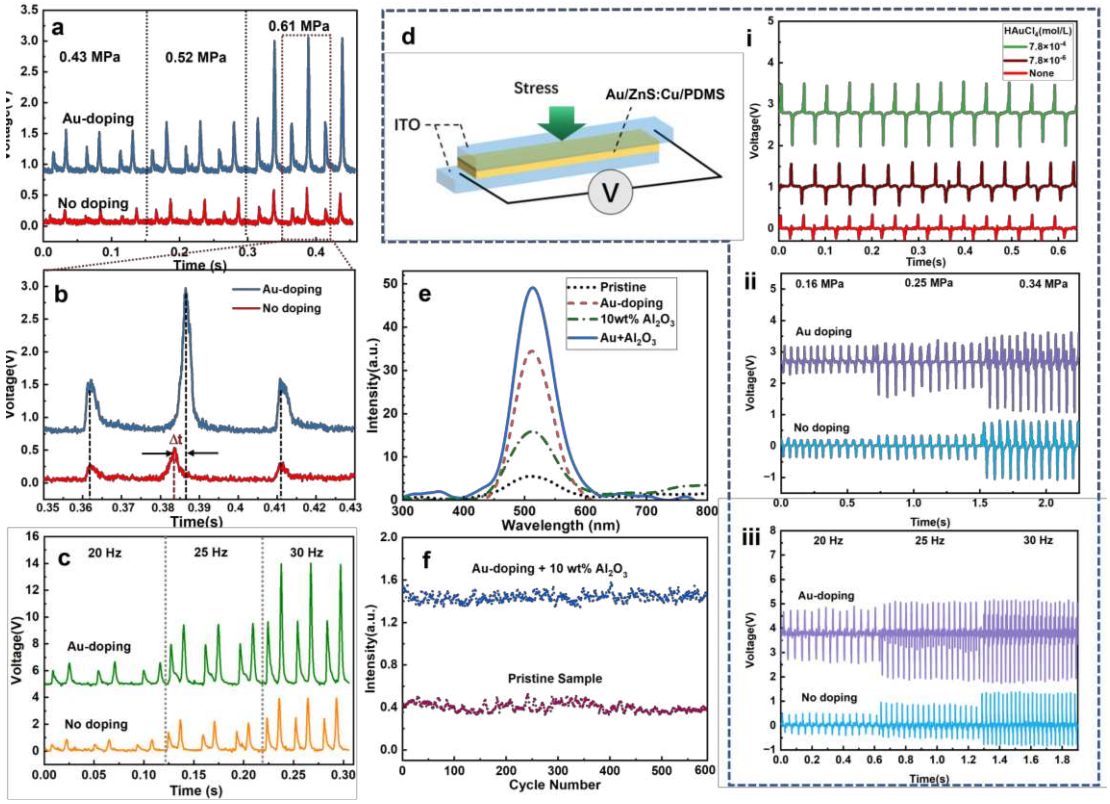


Fig. 4 Dynamic ML behavior, electromechanical transduction, and cyclic stability. a Time-resolved ML profiles under varying loads (0.43, 0.52, and 0.61 MPa) at 20 Hz showing synchronized peaks with monotonic intensity increase. **b** Expanded transient ML at 0.61 MPa revealing a $\Delta t \approx 3$ ms peak-to-peak delay in the unloading process. **c** ML profiles at 20, 25, and 30 Hz showing strain-rate dependence. **d** Triboelectric voltage under ITO-electrode configuration versus (**i**) $HAuCl_4$

concentration (0.25 MPa), (**ii**) compressive stress (20 Hz), and (**iii**) frequency (0.25 MPa), all showing higher amplitude for Au-doped hybrids. **e** ML spectra of pristine, Al_2O_3-doped, and Au/Al_2O_3 co-modified samples (20 wt% ZnS:Cu) showing synergistic M–E–O cascade. **f** ML peak intensity over 600 cycles at 0.6 MPa and 20 Hz, with only 2.78% fluctuation, demonstrating excellent cyclic stability attributed to robust Au–S covalent anchoring.

At 0.61 MPa, the Au-doped sample exhibits a distinct kinetic delay ($\Delta t \approx 3$ ms) in the unloading peak (Fig. 4b), directly reflecting the deepened trap states induced by the Au–S interfacial dipole. Upon stress release, the instantaneous collapse of triboelectric field leaves the dipole field intact, elevating the effective potential barrier and temporally gating carrier detrapping[48]. This gating mechanism is strictly charge-density dependent: the delay vanishes at lower pressures where interfacial charge accumulation is insufficient (Figs. S5 and S6), confirming that the kinetic bottleneck scales with the trapped carrier population. Furthermore, the ML peak intensity scales linearly with excitation frequency (20-30 Hz) under constant load (Fig. 4c), demonstrating rapid carrier replenishment and highly reproducible response kinetics—a critical prerequisite for high-bandwidth, real-time dynamic sensing.

The interfacial electromechanical transduction behavior was characterized using a double-electrode sandwich-structured test setup with indium tin oxide (ITO) electrodes (Fig. 4d). The measured triboelectric voltage outputs directly evidence the mechano-electrical (M–E) conversion pathway. In Fig. 4d(i), the voltage amplitude increases with Au precursor concentration (None < 7.8 μmol L^{-1} < 780 μmol L^{-1}) under periodic compression of 0.25 MPa at 20 Hz, demonstrating that Au incorporation enhances interfacial charge generation. As the applied pressure rises from 0.16 to 0.34 MPa (Fig. 4d(ii)) at 20 Hz, the peak-to-peak output voltage rises linearly, demonstrating a wide linear electromechanical response. Across the entire dynamic range, the Au-doped sample delivers higher voltage amplitude than the pristine, which originates from the

enhanced interfacial polarizability[42] and micro-capacitive charge-trapping effect of embedded Au nanoparticles[49], which magnify localized charge transfer. Furthermore, varying the excitation frequency from 20 to 30 Hz at 0.25 MPa reveals distinct dynamic response in Fig. 4d(iii). For the pristine film, the output voltage scales modestly and quasi-linearly across the spectrum. In contrast, the Au-doped hybrid exhibits a pronounced voltage elevation at 20 Hz, followed by a saturation behavior at 25-30 Hz. It is dictated by the intrinsic charge-relaxation time (RC constant) of the Au-induced micro-capacitive network[50] and the viscoelastic recovery limit of the elastomer under high-rate deformation[51]. Overall, Au doping not only doubles low-frequency mechanical sensitivity but also ensures robust electromechanical enhancement that underpins superior ML performance.

Steady-state ML spectra acquired under the standard test condition (0.6 MPa, 20 Hz, 20 wt% ZnS:Cu) are compared in Fig. 4e. Incorporation of rigid Al_2O_3 NPs (100nm, 10 wt%) yields a ~2.9-fold enhancement relative to the pristine, arising from the localized stress concentration effect[4,52]. Single Au-doping delivers a ~6-fold enhancement via LSPR coupling. When combined, the Au/Al_2O_3 co-modified hybrid achieves a remarkable ~9-fold overall ML enhancement through a synergistic M–E–O cascade: rigid Al_2O_3 maximizes triboelectric charge generation (M–E conversion), while Au NPs accelerate carrier radiative recombination via the Purcell effect (E-O conversion). The transient kinetic analysis (Fig. S8) reveals that while Al_2O_3 doping alone does not alter the unloading relaxation timescale, the introduction of Au NPs further delays the emission peak by ~1.5 ms. This kinetic signature confirms that the Au–S covalent interface deepens trap states and gates carrier release[16,53], operating synergistically with the Al_2O_3-mediated stress concentration to maximize the M–E–O cascade efficiency.

The operational stability of the triboelectric output was assessed over 600

consecutive cycles (Fig. 4f) by independent PMT monitoring. The Au/Al_2O_3 co-doped sample maintains a stable voltage amplitude (~1.5 V) with imperceptible attenuation, significantly outperforming the pristine control (~12.5% attenuation), which validates the effectiveness of the covalent Au–S anchoring in preventing interfacial degradation. The ML intensity under the same cycling conditions confirms comparable stability with only 2.78% intensity fluctuation over 600 cycles.

Flexible ML Devices and Multiscale Self-Powered Application Demonstrations

The enhanced ML emission and mechanical compliance of the hybrid elastomer enable diverse device applications across multiple scales. Fig. 5a presents a 4 × 6-pixel conical ML array on a flexible PDMS substrate. Each cone is 2.5 mm in diameter and 7 mm in height, and is composed of 20 wt% ZnS:Cu co-modified with the optimized Au anchoring and 10 wt% 100 nm Al_2O_3 NP fillers. The cone-tip induces geometric stress concentration, which amplifies local shear strain under dynamic mechanical stimuli and yields markedly higher transient ML intensity than planar counterparts. Based on this optimized conical array, a self-powered optical tachometer for ultra-low-visibility environments (<0.05 lx) was fabricated to demonstrate practical viability. Unlike conventional tachometers, which require external wiring and power supplies, the flexible ML array can be directly attached to the platform adjacent to a rotating motor pendulum, without adding extra weight, power consumption, or wiring complexity. Periodic lateral friction and impact from the rotating pendulum excite these conical pixels, producing dynamic green emission clearly visible to naked eyes in complete darkness. Stepwise 1 mm reductions in the gap between the pendulum and substrate produce a well-resolved gradient in emission brightness, as captured in three consecutive snapshots (Fig. 5a(i)–5a(iii)). Driven entirely by ambient mechanical energy, this device can also serve as a battery-free collision warning indicator for

aerospace systems and heavy machinery diagnostics.

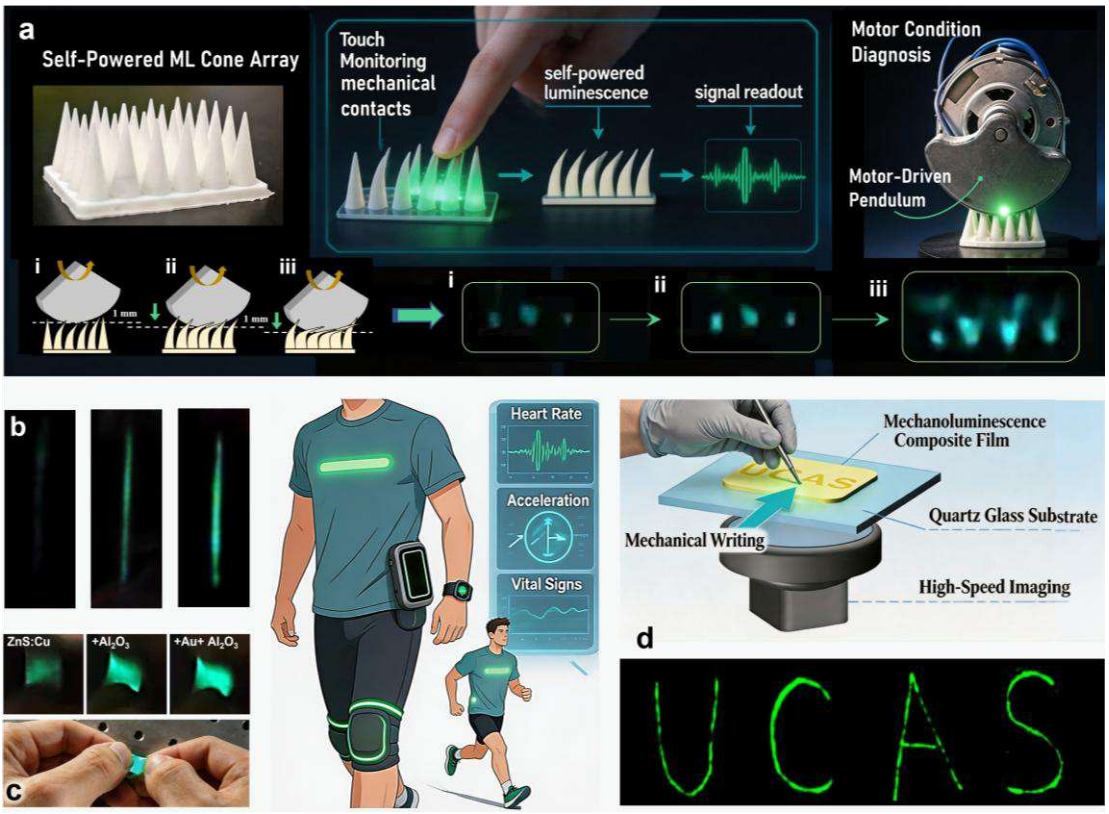


Fig. 5. Flexible ML devices and self-powered applications. a 4 × 6 conical ML array on PDMS with optimized 7.8 μmol L^{-1} Au and 10 wt% Al_2O_3, showing dynamic green emission under pendulum impact in darkness as a self-powered optical tachometer. **b** Uniaxial tensile testing of hybrid strips showing stepwise ML enhancement from pristine (20 wt% ZnS:Cu) to Au-anchored (7.8 μmol L^{-1}) to Au/ Al_2O_3 (10 wt% Al_2O_3) co-modified compositions. **c** Flexible ML flakes of 67 wt% ZnS:Cu loading: Peak emission snapshots and ambient-light visibility under uniaxial tensile loading. **d** Spatial pressure writing: "UCAS" pattern recorded by a 5 cm × 5 cm ML skin, demonstrating sub-millimeter resolution without lateral optical crosstalk.

The composition-structure synergy in device-level performance was demonstrated using stretched hybrid strips and flakes. Uniaxial tensile tests on three strips (50mm × 1mm × 1mm) compositions—pristine (20 wt%), Au-anchored (7.8 μmol L^{-1} Au), and Au/Al_2O_3 co-modified (7.8 μmol L^{-1} Au and 10 wt% Al_2O_3) ZnS:Cu/PDMS samples reveal a clear stepwise increase in emission intensity (Fig. 5b). The high stretchability

and brightness of the hybrid strips make them promising for self-powered strain sensing and durable wearable stress mapping in smart textiles and healthcare devices. For the flake configuration, increasing the phosphor loading to 67 wt% greatly boosts absolute brightness and visual contrast under stretching (Fig. 5c). Normalized ML intensities of 1, 3.28, and 4.56 correspond to pristine, Al_2O_3-doped, and Au/Al_2O_3 co-modified compositions (Fig. S7), respectively, demonstrating the stepwise enhancement from individual filler contributions to the synergistic M–E–O cascade. The co-modified hybrid flakes (67 wt% ZnS:Cu, 7.8 μmol L^{-1} Au precursor, 10 wt% Al_2O_3) exhibit bright green ML visible to naked eyes under ambient conditions (Lower row of Fig. 5c), confirming its practical viability for self-powered strain visualization, wearable optical sensing, and intuitive human-machine tactile interfaces.

Spatial pressure writing extends the functionality from macroscopic uniaxial stretching to localized, high-resolution contact-induced luminescence. Fig. 5d shows the test setup and handwriting visualization result for a flexible ML skin (5 cm × 5 cm × 1 mm) with the same composition as the above co-modified flake. The handwritten "UCAS" pattern, recorded from the back side by a synchronized high-definition camera, exhibits excellent trace contrast and high contour fidelity. Despite the high phosphor loading of 67 wt%, the in-situ formed covalent Au–S bond and preserved matrix resilience effectively prevent microscopic tearing, microcracking, and polymer delamination under the intense localized shear stress induced by the moving stylus. Notably, the luminescent traces show no lateral optical crosstalk or light diffusion, confirming sub-millimeter spatial resolution and high-fidelity M–O transduction. The combination of bright emission, high spatial stress resolution, and excellent mechanical compliance and deformability makes the ZnS:Cu/PDMS/Au/ Al_2O_3 hybrid elastomers a scalable platform for plasmonically enhanced mechanoluminescent devices, enabling

self-powered strain sensing, durable wearable stress mapping, and next-generation interactive smart skins.

Discussion

In summary, we report the first demonstration of plasmon-enhanced ML enabled by in-situ covalent Au–S anchoring of ZnS:Cu phosphors within a PDMS matrix. This interfacial engineering strategy simultaneously circumvents the metal-induced quenching–enhancement trade-off and cyclic interfacial delamination, effectively resolving the long-standing efficiency–durability–compliance trilemma in ML elastomers. The covalent Au–S bonds generate a localized interfacial dipole that stabilizes carriers in deep trap states and narrows the tunneling barrier under compression, while its persistent field acts as an "electronic lock" that temporally gates carrier release. Concurrently, the LSPR of anchored Au nanoparticles accelerates radiative recombination via the Purcell effect, as directly evidenced by the shortened ML lifetime (0.44 $\rightarrow$ 0.35 ms) and a lower-bound Purcell factor of $F_P > 1.26$. Unlike conventional approaches that merely increase carrier density or modulate trap depths, this mechanism selectively enhances the radiative probability of existing carriers. Furthermore, the embedded Au network amplifies the mechano-electrical transduction pathway by boosting interfacial polarizability and establishing a micro-capacitive charge-trapping architecture, yielding a ~5.5-fold increase in mechano–optical sensitivity and elevated triboelectric output. When integrated with Al_2O_3 stress concentrators, these effects converge into a synergistic mechano–electro–opticall cascade, delivering a ~9-fold ML enhancement at 20 wt% loading with exceptional cyclic stability (2.78% fluctuation over 600 cycles). The observed frequency-dependent saturation (25–30 Hz), governed by the Au-induced RC relaxation time and polymer

viscoelastic recovery, reveals a fundamental sensitivity–bandwidth trade-off in soft mechanophotonic systems. Collectively, this work clarifies the coupled charge dynamics in covalently anchored ML composites and establishes a quantitative interfacial design framework. The plasmonic–triboelectric synergy presented here is readily extensible to other wide-bandgap phosphors and flexible optoelectronic platforms, paving the way for self-powered tactile imaging, durable wearable sensors, and next-generation mechanophotonic devices that operate autonomously without external power or optical excitation.

Materials and Methods

Materials

ZnS:Cu powder (Duoshang Trading Co., LTD), Sylgard 184 PDMS base elastomer and curing agent (Dow Corning), $HAuCl_4 \cdot 3H_2O$ (≥99.9%, Shanghai Jizhi Biochemical Technology Co., LTD), Al_2O_3 nanoparticles (~100 nm, ≥99.99%, Sigma-Aldrich). PTFE molds (roughness of ≤0.1 μm, Suzhou Beike Polymer Materials Co., Ltd.) were custom-fabricated for sample preparation.

Fabrication of Hybrid Elastomeric samples

In the general process, ZnS:Cu phosphor was first mixed with $HAuCl_4$ ethanol solution, and the PDMS curing agent was then added and stirred for 5 min to allow complete in-situ reduction of Au^{3+} to Au^0. Subsequently, the PDMS base (base: curing agent mass ratio of 10:1) and optional Al_2O_3 nanoparticles (when co-doped) were added and stirred for an additional 5 min to achieve uniform dispersion. The mixture was transferred into different PTFE molds, degassed in a vacuum chamber, and cured at 90 °C for 30 min. After cooling to room temperature, various samples were obtained.

For the Au-doped disc sample with maximum ML enhancement factor, ZnS:Cu phosphor (0.03 g) was mixed with $HAuCl_4$ ethanol solution (7.8 μmol L^{-1}, 4.5 μL), followed by PDMS curing agent (0.012 g) and PDMS base (0.12 g). For device demonstrations, ZnS:Cu/PDMS/Au hybrid films were prepared with varying ZnS:Cu loadings (20-67 wt%) and $HAuCl_4$ concentration (7.8 μmol L^{-1}, 26 μL for 0.2 g ZnS:Cu). Al_2O_3 nanoparticles (10 wt% of total mixture) were co-doped into selected samples. The mixture was cast into conical array mold (cone radius 2.5 mm, height 7 mm; rectangular base: 20 × 10 × 0.5 mm), rectangular molds (20 × 10 × 1 mm), or other flat film mold. After curing and cooling, 6 × 4 conical arrays and sheet-shaped films were obtained. Additionally, a 300 μm-thick film was fabricated using a coating machine and cut into 1 mm-wide strips.

Material Characterization

Crystal structure was analyzed by X-ray diffraction (XRD, Rigaku SmartLab, Japan) using Cu Kα radiation (λ = 1.5406 Å) operated at 40 kV and 40 mA, over a 2θ range of 20-80° with a step size of 0.02°. Crystallite size was estimated using the Scherrer equation. Morphology and microstructure were characterized by a scanning electron microscopy (SEM, Hitachi SU8010, Japan). Elemental distribution was analyzed by energy-dispersive X-ray spectroscopy (EDS). Chemical states were examined using an X-ray photoelectron spectroscopy (XPS, AXIS Supra, Switzerland) with Al Kα radiation, calibrated with respect to the C 1s peak at 284.8 eV. Ultraviolet photoelectron spectroscopy (UPS) was performed with He I excitation (hv = 21.22 eV) to determine work functions and valence band maxima. UV-Vis absorption spectra were recorded using a spectrophotometer (Hitachi U3900, Japan). Photoluminescence (PL) spectra were recorded using a spectrofluorometer (Hitachi F7000, Japan) with a xenon lamp

excitation source (λ_{ex} = 400 nm). ML measurements were performed using a fluorescence spectrometer (Zolix Omni300i-RTS2, China) coupled with a mechanical vibration system. ML lifetime measurements were conducted via a single-pulse mechanical excitation by impact, with transient decay curves detected by a PMT (Hamamatsu H10722-20, Japan) and fitted with single-exponential model. Mechanical properties were evaluated using a universal testing machine (Instron 5967, USA), with the elastic modulus derived from the initial linear region of stress–strain curves. Triboelectric output was measured using a custom-built platform comprising a mechanical excitation system, conductive ITO electrodes, and an oscilloscope (Tektronix TBS 1000X, USA), with output voltage recorded under periodic mechanical stimulation at controlled pressure and frequency. Spatial pressure writing was recorded using a high-definition camera (Hualteng Vision HT-FA0816, 2.3 MP, 165 fps, 1.1-inch sensor, 8 mm lens, China).

Device Demonstrations

Cone-arrayed ZnS:Cu/PDMS/Au/Al_2O_3 composites were fixed onto a flat substrate facing an electrically driven pendulum operated at 5 Hz, with separation distance reduced by 1 mm in each measurement. Strip-shaped and rectangular samples were stretched to approximately 50% strain and released without external intervention. The ML photos were recorded using a smartphone camera in high-frame-rate mode. For handwriting visualization, a 300-μm-thick composite film was fabricated, and the handwriting of "UCAS" was written using a stylus tip under continuous sliding, with luminescence recorded by the high-definition camera.

Acknowledgements

The authors acknowledge financial support from the Key Project of the National Natural Science Foundation of China (52532007) and National Natural Science Foundation of China (12374398).

Author details

[1]School of Optoelectronics, University of Chinese Academy of Sciences (UCAS), Beijing 101408, China

[2]State Key Laboratory of New Ceramic Materials, Tsinghua University, Beijing 100084, China

[3]School of Materials Science and Engineering, Tsinghua University, Beijing 100084, China

[4]Aerospace Information Research Institute, Chinese Academy of Sciences, No. 9 Dengzhuang South Road, Haidian District, Beijing 100094, China

Author contributions

Y.T.Q. and J.X.H. contributed equally to this work. G.Y.D. conceived and supervised the project, while T.Z.Z. and J.Z. provided additional strategic guidance. Y.T.Q. and J.X.H. performed the experiments with help from H.N.S., X.L.S., Z.Z., W.G.T. and Y.T.Q. carried out the spectral measurements, verified result reproducibility, and contributed to manuscript writing. J.X.H. performed the simulations and analyzed the computational data. G.Y.D. contributed to editing and revision. G.Y.D., T.Z.Z. and J.Z. served as corresponding authors and contributed to manuscript review. All authors discussed the results and approved the final version of the manuscript.

Data availability

All the data supporting the findings of this study are presented within the article and its Supplementary Information. Additional data related to this paper are available from the corresponding authors upon request.

Conflict of interest

The authors declare no competing interests.

Supplementary information accompanies the manuscript on the Light: Science & Applications website.

References

1 Wu, S., Wang, S., Shao, Z., Wang, Y. & Xiong, P. Self-powered near-infrared mechanoluminescence through MgO/MgF2 piezo-photonic heterojunctions. *Nature Communications* **16**, 8912, doi:10.1038/s41467-025-63980-4 (2025).

2 Li, W. *et al.* Micro-Strain Responsive Near-Infrared Mechanoluminescence for Potential Nondestructive Artificial Joint Stress Imaging. *Adv. Mater.* **38**, e05360, doi:10.1002/adma.202505360 (2026).

3 Fang, Z. *et al.* Self-recoverable mechanoluminescence in simple oxides: Al2O3:Cr. *Light: Science & Applications* **15**, 200, doi:10.1038/s41377-026-02274-w (2026).

4 Zhuang, Y. *et al.* Visualizing Dynamic Mechanical Actions with High Sensitivity and High Resolution by Near-Distance Mechanoluminescence Imaging. *Adv. Mater. Processes* **34**, 2202864, doi:10.1002/adma.202202864 (2022).

5 Li, L. *et al.* Stress-Triggered Mechanoluminescence in ZnO-Based Heterojunction for Flexible and Stretchable Mechano-Optics. *Adv. Funct. Mater.* **33**, 2301372, doi:10.1002/adfm.202301372 (2023).

6 Liu, H. *et al.* Realizing Red Mechanoluminescence of ZnS: Mn2+ Through Ferromagnetic Coupling. *Adv. Funct. Mater.* **34**, 2314422, doi:10.1002/adfm.202314422 (2024).

7 Moon Jeong, S., Song, S., Lee, S.-K. & Choi, B. J. A. P. L. Mechanically driven light-generator with high durability. *Appl. Phys. Lett.* **102**, 051110, doi:10.1063/1.4791689 (2013).

8 Qasem, A., Xiong, P., Ma, Z., Peng, M. & Yang, Z. Recent Advances in Mechanoluminescence of Doped Zinc Sulfides. *Laser Photonics Rev.* **15**, 2100276, doi:10.1002/lpor.202100276 (2021).

9 Wang, Z. *et al.* A mechanoluminescent material, ZnS:Mn,Li, with enhanced brightness for visualizing dental occlusion. *Anal. Bioanal. Chem.* **416**, 3975-3984, doi:10.1007/s00216-023-04968-1 (2024).

10 Lv, X. *et al.* Self-powered mechanoluminescent elastomer for solar-blind ultraviolet emission. *Light Sci. Appl.* **15**, 61, doi:10.1038/s41377-025-02131-2 (2026).

11 Tao, W. *et al.* Flexible mechano–optical sensors from mechanoluminescence to mechanoplasmonics: designs, applications, and prospects. *Journal of Materials Chemistry C* **13**, 2058-2090, doi:10.1039/d4tc04762a (2025).

12 Runowski, M. *et al.* Sound, Force and Light Induced Emissions from Er3+-Mn2+ Doped ZnS/CaZnOS Heterostructure for Remote Temperature Monitoring via Photo- and Mechanoluminescence. *Adv. Mater.* **37**, e10117, doi:10.1002/adma.202510117 (2025).

13 Sohn, K.-S., Timilsina, S., Singh, S. P., Lee, J.-W. & Kim, J. S. A Mechanoluminescent ZnS:Cu/Rhodamine/SiO2/PDMS and Piezoresistive CNT/PDMS Hybrid Sensor: Red-Light Emission and a Standardized Strain

Quantification. *ACS Appl. Mater. Interfaces* **8**, 34777-34783, doi:10.1021/acsami.6b12931 (2016).

14 Yu, Y. *et al.* Investigation of the Reinforcement Mechanism and Impact Resistance of Carbon Hollow Microsphere-Reinforced PDMS Composites. *Polymers* **17**, 2087, doi:10.3390/polym17152087 (2025).

15 Wong, M.-C., Chen, L., Tsang, M.-K., Zhang, Y. & Hao, J. Magnetic-Induced Luminescence from Flexible Composite Laminates by Coupling Magnetic Field to Piezophotonic Effect. *Adv. Mater.* **27**, 4488-4495, doi:10.1002/adma.201502015 (2015).

16 Wang, F. *et al.* Mechanoluminescence enhancement of ZnS:Cu,Mn with piezotronic effect induced trap-depth reduction originated from PVDF ferroelectric film. *Nano Energy* **63**, 103861, doi:10.1016/j.nanoen.2019.103861 (2019).

17 Franklin, D., George, M., Fraser, J. & Chanda, D. Atomic Layer Deposition Tuning of Subwavelength Aluminum Grating for Angle-Insensitive Plasmonic Color. *ACS Appl. Nano Mater.* **1**, 5210-5216, doi:10.1021/acsanm.8b01147 (2018).

18 Cai, Y.-Y. *et al.* Photoluminescence of Gold Nanorods: Purcell Effect Enhanced Emission from Hot Carriers. *ACS Nano* **12**, 976-985, doi:10.1021/acsnano.7b07402 (2017).

19 Bao, X. *et al.* Giant Out-of-Plane Exciton Emission Enhancement in Two-Dimensional Indium Selenide via a Plasmonic Nanocavity. *Nano Lett.* **23**, 3716-

3723, doi:10.1021/acs.nanolett.2c04902 (2023).

20 Tseng, M. L. *et al.* Two-Dimensional Active Tuning of an Aluminum Plasmonic Array for Full-Spectrum Response. *Nano Lett.* **17**, 6034-6039, doi:10.1021/acs.nanolett.7b02350 (2017).

21 Qin, Y. *et al.* Boosting fluorescence efficiency via filling technique prepared photonic crystal composites. *Sci. Rep.* **15**, 19990, doi:10.1038/s41598-025-04296-7 (2025).

22 Liang, C. *et al.* Gold Nanorod Size-Dependent Fluorescence Enhancement for Ultrasensitive Fluoroimmunoassays. *ACS Appl. Mater. Interfaces* **13**, 11414-11423, doi:10.1021/acsami.0c20303 (2021).

23 Tao, W. *et al.* Flexible mechano–optical sensors from mechanoluminescence to mechanoplasmonics: designs, applications, and prospects. *J. Mater. Chem. C* **13**, 2058-2090, doi:10.1039/d4tc04762a (2025).

24 Gupta, R., Nagamanasa, H. K., Ganapathy, R. & Kulkarni, G. U. Viscoelastic nature of Au nanoparticle–PDMS nanocomposite gels. *Bull. Mater. Sci.* **38**, 817-823, doi:10.1007/s12034-015-0957-1 (2015).

25 Hanosh, S., K, M. & George, S. D. Plasmonic Slippery Surface for Surface-Enhanced Raman Spectroscopy and Protein Adsorption Inhibition. *Anal. Chem.* **97**, 2610-2617, doi:10.1021/acs.analchem.4c01844 (2025).

26 Love, J. C., Estroff, L. A., Kriebel, J. K., Nuzzo, R. G. & Whitesides, G. M. Self-Assembled Monolayers of Thiolates on Metals as a Form of Nanotechnology. *Chem. Rev.* **105**, 1103-1170, doi:10.1021/cr0300789 (2005).

27 Włodarski, M., Nowak, M. P., Putkonen, M., Nyga, P. & Norek, M. Surface Modification of ZnO Nanotubes by Ag and Au Coatings of Variable Thickness: Systematic Analysis of the Factors Leading to UV Light Emission Enhancement. *ACS Omega* **9**, 1670-1682, doi:10.1021/acsomega.3c08253 (2023).

28 Feng, Y. *et al.* A Soft Mechanoluminescent Skin for High-Resolution Optical Tactile Sensing in Human–Machine Interaction. *Adv. Sci.* **13**, e75507, doi:10.1002/advs.75507 (2026).

29 Qian, X. *et al.* Printable Skin-Driven Mechanoluminescence Devices via Nanodoped Matrix Modification. *Adv. Mater.* **30**, 1800291, doi:10.1002/adma.201800291 (2018).

30 Joint Committee on Powder Diffraction Standards. (Joint Committee on Powder Diffraction Standards, Swarthmore, PA, 1986).

31 Wang, W., Wang, S., Gu, Y., Zhou, J. & Zhang, J. Contact-separation-induced self-recoverable mechanoluminescence of CaF2:Tb3+/PDMS elastomer. *Nat. Commun.* **15**, 2014, doi:10.1038/s41467-024-46432-3 (2024).

32 Pan, X. *et al.* Quantifying the interfacial triboelectricity in inorganic-organic composite mechanoluminescent materials. *Nat. Commun.* **15**, 2673, doi:10.1038/s41467-024-46900-w (2024).

33 Scherrer, P. Bestimmung der Grösse und der inneren Struktur von Kolloidteilchen mittels Röntgengenstrahlen. *Nachrichten von der Gesellschaft der Wissenschaften zu Göttingen, Mathematisch-Physikalische Klasse* **1918**, 98-100 (1918).

34 Wang, Z. *et al.* Size and Structural Control of Mechanoluminescent ZnS:Mn2+ Nanocrystals for Optogenetic Neuromodulation. *ACS Nano* **19**, 19340-19352, doi:10.1021/acsnano.5c03057 (2025).

35 Bol, A. A., Ferwerda, J., Bergwerff, J. A. & Meijerink, A. Luminescence of nanocrystalline ZnS:Cu2+. *J. Lumin.* **99**, 325-334, doi:10.1016/S0022-2313(02)00350-2 (2002).

36 Zhang, Q., Xu, J.-J., Liu, Y. & Chen, H.-Y. In-situ synthesis of poly(dimethylsiloxane)–gold nanoparticles composite films and its application in microfluidic systems. *Lab on a Chip* **8**, 352-357, doi:10.1039/b716295m (2008).

37 SadAbadi, H., Badilescu, S., Packirisamy, M. & Wüthrich, R. Integration of gold nanoparticles in PDMS microfluidics for lab-on-a-chip plasmonic biosensing of growth hormones. *Biosens. Bioelectron.* **44**, 77-84, doi:10.1016/j.bios.2013.01.016 (2013).

38 Casaletto, M. P., Longo, A., Martorana, A., Prestianni, A. & Venezia, A. M. XPS study of supported gold catalysts: the role of Au0 and Au+δ species as active sites. *Surf. Interface Anal.* **38**, 215-218, doi:10.1002/sia.2180 (2006).

39 Lee, A. Y. *et al.* Development of the NIST X-ray Photoelectron Spectroscopy (XPS) Database, Version 5. *Data Science Journal* **23**, 45, doi:10.5334/dsj-2024-045 (2024).

40 Rodriguez, J. A. *et al.* Coverage Effects and the Nature of the Metal−Sulfur Bond in S/Au(111): High-Resolution Photoemission and Density-Functional

Studies. *J. Am. Chem. Soc.* **125**, 276-285, doi:10.1021/ja021007e (2002).

41 Nuzzo, R. G. & Allara, D. L. Adsorption of bifunctional organic disulfides on gold surfaces. *J. Am. Chem. Soc.* **105**, 4481-4483, doi:10.1021/ja00351a063 (1983).

42 Kwak, M. S., Park, Y.-J., Kim, M. P. & Ko, H. Interfacial Polarization for High-Performance Triboelectric Devices: Principles, Strategies, and Applications. *ACS Applied Materials & Interfaces* **17**, 37336-37352, doi:10.1021/acsami.5c03133 (2025).

43 Haiss, W., Thanh, N. T. K., Aveyard, J. & Fernig, D. G. Determination of Size and Concentration of Gold Nanoparticles from UV−Vis Spectra. *Anal. Chem.* **79**, 4215-4221, doi:10.1021/ac0702084 (2007).

44 Novotny, L. & Hecht, B. *Principles of Nano-Optics*. 3 edn, (Cambridge University Press, 2025).

45 Gelbing, P., Jelken, J., Foschum, F. & Kienle, A. Investigating the Interplay of Absorption and Scattering in Phosphor-Converted LEDs Using a GPU-Accelerated Monte Carlo Framework. *Photonics* **13**, 206, doi:10.3390/photonics13020206 (2026).

46 Lee, G. *et al.* Interfacial Triboelectricity Lights Up Phosphor-Polymer Elastic Composites: Unraveling the Mechanism of Mechanoluminescence in Zinc Sulfide Microparticle-Embedded Polydimethylsiloxane Films. *Small* **20**, 2307089, doi:10.1002/smll.202307089 (2024).

47 Canneson, D. *et al.* Strong Purcell effect observed in single thick-shell

CdSe/CdS nanocrystals coupled to localized surface plasmons. *Physical Review B* **84**, 245423, doi:10.1103/PhysRevB.84.245423 (2011).

48 Du, J. *et al.* Pushing Trap-Controlled Persistent Luminescence Materials toward Multi-Responsive Smart Platforms: Recent Advances, Mechanism, and Frontier Applications. *Adv. Mater.* **36**, 2314083, doi:10.1002/adma.202314083 (2024).

49 Hu, Y., Wang, F., Ma, Y., Ma, S. & Wang, L. Recent Advances in Polyvinylidene Fluoride with Multifunctional Properties in Nanogenerators. *Small* **21**, 2412476, doi:10.1002/smll.202412476 (2025).

50 Carroll, B., Cheng, S. & Sokolov, A. P. Analyzing the Interfacial Layer Properties in Polymer Nanocomposites by Broadband Dielectric Spectroscopy. *Macromolecules* **50**, 6149-6163, doi:10.1021/acs.macromol.7b00825 (2017).

51 Chen, X., Jiang, T. & Wang, Z. L. Modeling a dielectric elastomer as driven by triboelectric nanogenerator. *Appl. Phys. Lett.* **110**, 033505, doi:10.1063/1.4974143 (2017).

52 Li, Y. *et al.* Optimization of mechanoluminescence properties of ZnS:M@Al2O3-PDMS (M = Mn, Cu) composites based on synergistic effects of temperature and composition. *Opt. Mater.* **167**, 117331, doi:10.1016/j.optmat.2025.117331 (2025).

53 Li, Y., Li, Z., Sun, H., Kwok, K. W. & Zhou, G. Deep trap assisting elastico-mechanoluminescence in diphase non-piezoelectrics induced by tunneling effect. *Appl. Phys. Lett.* **123**, 192902, doi:10.1063/5.0170880 (2023).

Supplementary Files

This is a list of supplementary files associated with this preprint. Click to download.

- SupplyInformation.docx